Quantum anomalous, spin, and valley Hall effects in pentalayer rhombohedral graphene moiré superlattices

Koji Kudo,[1] Ryota Nakai,[1,2] and Kentaro Nomura[1]
[1]*Department of Physics, Kyushu University, Fukuoka 819-0395, Japan*
[2]*RIKEN Center for Quantum Computing (RQC), Wako, Saitama 351-0198, Japan*

(Received 9 July 2024; revised 30 October 2024; accepted 25 November 2024; published 23 December 2024)

Recent experiments on pentalayer rhombohedral graphene moiré superlattices have observed the quantum anomalous Hall effect at a moiré filling factor of $\nu = 1$ and various fractional values. These phenomena are attributed to a flat Chern band induced by electron-electron interactions. In this study, we demonstrate that at $\nu = 2$, many-body effects can lead to the emergence of quantum spin Hall and quantum valley Hall states, in addition to the quantum anomalous Hall state, even in the absence of spin-orbit coupling or valley-dependent potentials. These three topological states can be selectively induced by the application and manipulation of a magnetic field. Furthermore, we show that at $\nu = 3$ and 4, the ground state can be a combination of topologically trivial and nontrivial states, unlike the cases of $\nu = 1$ and 2. This contrasts with the conventional quantum Hall effect in graphene where the ground state at filling factor ν is given as the particle-hole counterpart at $4 - \nu$.

DOI: 10.1103/PhysRevB.110.245135

I. INTRODUCTION

The recent discovery of both integer and fractional quantum anomalous Hall (QAH) effects in moiré materials represents a major milestone in condensed matter physics [1–5]. Moiré materials provide a fertile ground for exploring strong interaction effects [6,7], leading to the emergence of various symmetry-broken phases such as superconductivity and Wigner crystals [8–12], as well as topological phases [13–18]. The QAH effect is particularly intriguing because it arises from the interplay between symmetry breaking and topology, resulting in a quantized Hall conductance even in the absence of external magnetic fields [19–22]. Both integer and fractional QAH effects were first observed in twisted bilayer $MoTe_2$ [1–4], marking a significant achievement in the study of moiré materials. More recently, these phenomena have been reported in pentalayer rhombohedral graphene on hexagonal boron nitride (hBN) at a moiré filling factor of $\nu = 1$ and at various fractional values [5]. This breakthrough has spurred extensive theoretical investigations [23–45].

The emergence of Chern bands in pentalayer rhombohedral graphene on hBN can be attributed to the combined effects of layer stacking, moiré structure, and many-body interactions [31–35]. The band touching at the charge-neutral point of multilayer rhombohedral graphene [46–58] becomes increasingly flat (approximately $\sim k^{N_L}$ with wave number k) as the number of stacked layers N_L increases [59]. The moiré superlattice structure, resulting from the lattice mismatch between pentalayer graphene and hBN [60,61], reduces the graphene's Brillouin zone (BZ) into moiré BZ, narrowing the band width. Ultimately, electron-electron interactions play a crucial role in isolating a Chern band from the rest of the moiré bands. Specifically, Hartree-Fock (HF) analysis has revealed the emergence of an isolated and nearly flat Chern band at $\nu = 1$ [31–35], which does not appear in the absence of electron interactions. This mechanism is believed to underlie the observed $\nu = 1$ and fractional QAH states [5,31–35].

Traditionally, quantum Hall physics [18,62–79] relies on *noninteracting* topological bands, such as Landau levels, as a foundation. However, pentalayer rhombohedral graphene on hBN deviates from this noninteracting framework, indicating the potential for interaction-driven exotic phases beyond the conventional quantum Hall paradigm, even at integer fillings. This observation prompts an investigation into pentalayer rhombohedral graphene on hBN at integer fillings other than $\nu = 1$, which have not yet been explored experimentally under a sufficiently strong displacement field [5].

In this study, we demonstrate that pentalayer rhombohedral graphene at $\nu = 2$ can give rise to quantum spin Hall (QSH) and quantum valley Hall (QVH) states, in addition to the QAH state, even in the absence of spin-orbit coupling or valley-dependent potentials. These states emerge purely from many-body effects, which is a kind of a topological Mott insulator proposed in Ref. [80]. Our self-consistent HF calculations show that the QAH, QSH, and QVH states at $\nu = 2$ are degenerate but distinguishable by their magnetization magnitudes. This distinction allows for the selective induction of one of these states by applying and tilting magnetic fields, as illustrated in Fig. 1(a). The emergence of these three states can be understood by analogy to the $\nu = 1$ case: the emergent Chern band at $\nu = 1$ spontaneously selects the valley K or K' and spin $\uparrow, \downarrow$, where the band Chern number is $+1$ for K and -1 for K' [31–35]. At $\nu = 2$, the ground state comprises two Chern bands selected from $(K\uparrow, K\downarrow, K'\uparrow, K'\downarrow)$ [see Fig. 1(b)]. Different combinations of the four degrees of freedom result in distinct topological states, leading to QAH, QSH, and QVH effects. The possible combinations are detailed in Table I.

Notably, the empirical rule of forming the lowest energy state by occupying the Chern bands does not hold at $\nu = 3$

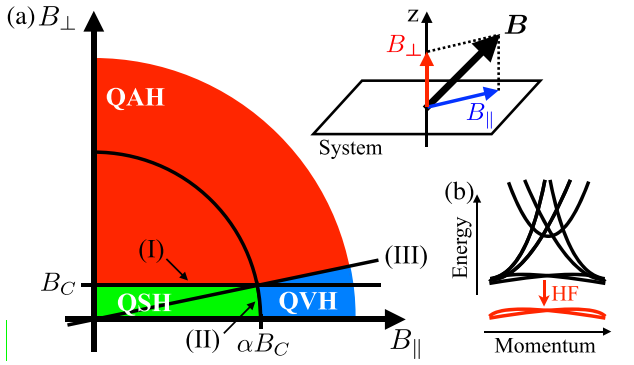

FIG. 1. (a) Lowest energy state as a function of the in-plane and out-of-plane components $(B_\parallel, B_\perp)$ of the magnetic field $\boldsymbol{B}$. The boundaries are defined as follows: (I) QAH versus QSH transition occurs at $B_\perp = B_C$, where B_C is the critical magnetic field such that $B_C \times M_{\rm orb}^{z(\rm QAH)}$, with $M_{\rm orb}^z$ defined in Eq. (1), equals the magnetostatic energy of the QAH state. (II) QVH versus QSH boundary at $|\boldsymbol{B}| = \alpha B_C$ with $\alpha = 4.9$ [refer to Eq. (2)]. (III) QVH versus QAH transition described by $\alpha B_\perp = |\boldsymbol{B}|$. (b) Schematic of the band structure with and without the Hartree-Fock (HF) interaction at $\nu = 2$. The HF interaction results in two isolated bands, as demonstrated in Fig. 2 below. The choice among the valley and spin–$(K\uparrow, K\downarrow, K'\uparrow, K'\downarrow)$–does not influence the total energy. All possible occupancies are summarized in Table I.

and $\nu = 4$. At these filling factors, the ground state can be a combination of topologically trivial and nontrivial states. This occurs because the spatial charge density distributions of these states interlock; the localized density of the trivial state fits into the low-density regions of the topological states. This phenomenon, driven by many-body interactions, contrasts with the conventional quantum Hall effect in graphene where the ground state at filling factor ν is given as the particle-hole counterpart at $4 - \nu$.

TABLE I. Possible occupancy of the four degrees of freedom at $\nu = 2$, yielding ${}_4C_2 = 6$ states. The charge Chern number C_c sums the band Chern numbers, whereas the spin (valley) Chern number C_s (C_v) represents the difference concerning the spin (valley). [Here, the band Chern number for the valley K (K') is $+1$ (-1)]. The three types of states–quantum anomalous Hall (QAH), quantum spin Hall (QSH), and quantum valley Hall (QVH)–are distinguished. The magnetization results in Fig. 3 are also summarized, with ○ indicating finite magnetization. Note that our QSH state also supports the QVH effect [81].

	Occupancy						Magnetization	
#	$K\uparrow$	$K\downarrow$	$K'\uparrow$	$K'\downarrow$	(C_c, C_s, C_v)	Type	Orbital	Spin
1	✓	✓	×	×	(2,0,2)	QAH	○	
2	×	×	✓	✓	(−2,0,2)			
3	✓	×	×	✓	(0,2,2)	QSH		
4	×	✓	✓	×	(0,−2,2)			
5	✓	×	✓	×	(0,0,2)	QVH		○
6	×	✓	×	✓	(0,0,2)			

II. MODEL

For numerical analysis, an effective continuum model is used [31,33]. The starting point is the tight-binding Hamiltonian of pentalayer rhombohedral graphene, including both intralayer and interlayer hoppings as well as the interlayer potential difference [see Appendix A]. Using a standard approach to reach the continuum limit, the effective Hamiltonian near the charge-neutral point is derived: $H_{R5G} = \sum_{\boldsymbol{k}} \boldsymbol{c}^\dagger(\boldsymbol{k}) h_{R5G}(\boldsymbol{k}) \boldsymbol{c}(\boldsymbol{k})$ for a given valley and spin, where $\boldsymbol{c}^\dagger = (c_{A_1}^\dagger, c_{B_1}^\dagger, c_{A_2}^\dagger, \ldots, c_{B_5}^\dagger)$ and $c_{X_l}^\dagger$ is a creation operator for the sublattice $X = A, B$ on the layer $l = 1, 2, \ldots, 5$. The matrix $h_{R5G}(\boldsymbol{k})$ is ten-dimensional. System parameters are set to match experimental conditions for the $\nu = 1$ QAH effect [5,31,33,82]; see Appendix A.

Stacking graphene on hBN induces a moiré superlattice structure due to lattice mismatch. In this study, the twist angle is set to 0.77° to align with the experimental conditions described in Ref. [5]. Within the effective continuum model, the impact of hBN is represented by a local potential $v(\boldsymbol{r})$ within the bottom graphene layer [60,61] (see Appendix B for more details). The second quantized form of this potential is $V_{\rm hBN} = \sum_{\boldsymbol{k}} \sum_{m_1 m_2} \tilde{\boldsymbol{c}}^\dagger(\boldsymbol{k} + m_1\boldsymbol{G}_1 + m_2\boldsymbol{G}_2) v(m_1, m_2) \tilde{\boldsymbol{c}}(\boldsymbol{k})$, where $\tilde{\boldsymbol{c}}^\dagger = (c_{A_1}^\dagger, c_{B_1}^\dagger)$, $\boldsymbol{G}_1$ and $\boldsymbol{G}_2$ are the moiré reciprocal lattice vectors, and $v(m_1, m_2)$ is the Fourier coefficient of $v(\boldsymbol{r})$. In the numerical calculations, the summation $\sum_{\boldsymbol{k}} \sum_{m_1 m_2}$ is confined to the first and second moiré BZs.

The effective noninteracting Hamiltonian is obtained as $H_{R5G} + V_{\rm hBN}$. To incorporate many-body effects, the HF interaction is added. The original interaction term is $H_{\rm int} = (1/2S) \sum_{\boldsymbol{k}\boldsymbol{k}'\boldsymbol{q}} \sum_{ZZ'} V_C(\boldsymbol{q}) c_Z^\dagger(\boldsymbol{k} + \boldsymbol{q}) c_{Z'}^\dagger(\boldsymbol{k}' - \boldsymbol{q}) c_{Z'}(\boldsymbol{k}') c_Z(\boldsymbol{k})$, where S is the area of the system, and Z and Z' represent the spin, valley, sublattice, and layer indices. The dual gate-screened Coulomb interaction used is $V_C(\boldsymbol{q}) = e^2/(2\epsilon_0\epsilon_r q) \tanh(q d_s)$ for $\boldsymbol{q} \neq \boldsymbol{0}$ and $V_C(\boldsymbol{q} = \boldsymbol{0}) = 0$, with $d_s = 25$ nm as the gate distance and $\epsilon_r = 5$ as the dielectric constant [33]. More details on the HF interaction can be found in Appendix C. To reduce computational cost, the calculations are performed within the subspace of the first three noninteracting conduction bands for each valley and spin. The system with 24×24 moiré unit cell is used unless otherwise specified.

III. BAND STRUCTURE

The self-consistent HF calculation assumes conservation of both spin and valley. The spin conservation assumption is valid due to the SU(2) spin-rotational symmetry of the HF Hamiltonian. Although valley conservation is nontrivial at this moment, we assume it based on the HF results at $\nu = 1$ [35].

Figures 2(a) and 2(b) display the HF band structures of lowest energy solutions, calculated by fixing the particle number at $\nu = 2$. (To be precise, the state in Fig. 2(b) has a lower energy than that in (a) by 10^{-8} eV per particle. Given the small difference, we consider the two states to be degenerate [84]). In Fig. 2(a), the occupied two lowest bands, distinctly separated from other conduction bands, exhibit $(K\uparrow, K'\downarrow)$ with the band Chern numbers $C = (1, -1)$, corresponding to state #3 (QSH) in Table I. In Fig. 2(b), the two lowest bands exhibit $(K\uparrow, K\downarrow)$ with band Chern numbers $C = (1, 1)$,

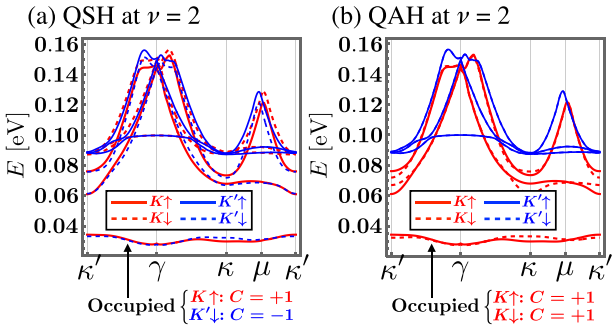

FIG. 2. Band structures at $\nu = 2$ for the lowest energy Hartree-Fock solutions (refer to Ref. [84]). Greek letters denote the high-symmetric points in the moiré BZ. Colors and line styles denote valley and spin properties. (a) and (b) correspond to the states #3 (QSH) and #1 (QAH) listed in Table I, respectively. In the calculation for (b), a small "valley Zeeman term" is introduced to favor valley K (refer to Ref. [83]). The HF analysis is performed with the particle number fixed at $\nu = 2$.

corresponding to state #1 (QAH) in Table I. Because the HF Hamiltonian maintains symmetry for spin flipping in each valley, these two results indicate that the QAH, QSH, and QVH states in Table I are all degenerate ground states. [For example, state #5 (QVH) can be obtained by flipping the spin for K' in state #3]. These states do not emerge in the absence of the HF interaction. Their emergence results from many-body effects.

IV. LOWEST ENERGY STATE

We now analyze the selectivity among the QAH, QSH, and QVH states listed in Table I under three specific conditions: (i) In-plane magnetic field, (ii) Out-of-plane magnetic field, and (iii) Absence of magnetic field.

(i) In-plane magnetic field: Under an in-plane magnetic field, the field favors a state with the largest in-plane magnetization, which is the QVH state due to its spin polarization. The strength of the spin magnetization for each state is quantified as follows: $M_{\text{spin}}^{(\text{QVH})} = g\mu_B n_e$ and $M_{\text{spin}}^{(\text{QAH})} = M_{\text{spin}}^{(\text{QSH})} = 0$. Here, the g factor is assumed to be 2, μ_B denotes the Bohr magneton, and n_e represents the electron density. Note that the orbital magnetization has no in-plane component.

(ii) Out-of-plane magnetic field: For an out-of-plane magnetic field, both spin and orbital magnetizations are relevant. The orbital magnetization in the z direction is calculated using the expression [85–88]:

$$M_{\text{orb}}^z = \frac{e}{2\hbar i}\int^{\mu}\frac{dk^2}{(2\pi)^2}\left\langle\frac{\partial u}{\partial \boldsymbol{k}}\right|\times\left(H(\boldsymbol{k})+E(\boldsymbol{k})-2\mu\right)\left|\frac{\partial u}{\partial \boldsymbol{k}}\right\rangle, \tag{1}$$

where $u(\boldsymbol{k})$ and $E(\boldsymbol{k})$ are an eigenstate and eigenenergy of the Bloch Hamiltonian $H(\boldsymbol{k})$, respectively. The integral encompasses states with energies below the chemical potential μ. (In numerical calculations, μ is positioned at the top of the valence bands). In Fig. 3, we illustrate the orbital magnetization M_{orb}^z for states #1 and #3 from Table I, representing the QAH and QSH states, respectively. Due to symmetry, the QVH state displays the same M_{orb}^z as the QSH state. The finite-size scaling analysis presented in the figure reveals that the QSH state exhibits zero magnetization, $M_{\text{orb}}^{z(\text{QSH})} + M_{\text{spin}}^{(\text{QSH})} = 0$, while the QAH state manifests a magnetization approximately five times greater than that of the QVH state:

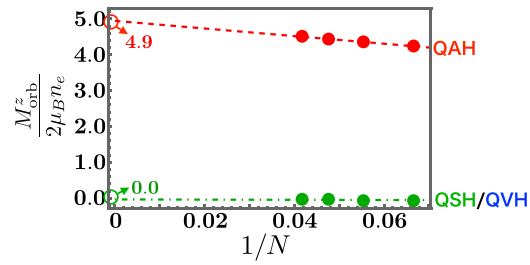

FIG. 3. Orbital magnetization M_{orb}^z, expressed in units of $2\mu_B n_e$ where μ_B is the Bohr magneton and n_e is the electron density, for $N \times N$ moiré unit cells. The states #1 and #3 from Table I serve as representatives for the QAH and QSH states, respectively. The dashed lines represent a linear approximation. Due to symmetry, the QSH and QVH states exhibit identical values of M_{orb}^z.

$$\frac{M_{\text{orb}}^{z(\text{QAH})} + M_{\text{spin}}^{(\text{QAH})}}{M_{\text{orb}}^{z(\text{QVH})} + M_{\text{spin}}^{(\text{QVH})}} \approx 4.9 \equiv \alpha. \tag{2}$$

Consequently, a QAH state is favored for the out-of-plane magnetic field.

(iii) No magnetic field: In the absence of a magnetic field, the state with the smallest magnetization is favored to minimize the magnetostatic energy. Therefore, the QSH state becomes the preferred state. (At this point, it is not possible to energetically differentiate between states #3 and #4 in Table I. However, considering weak spin-orbit interactions in real systems, either of these states should be favored).

This argument implies that the QSH state, realized in the absence of a magnetic field, transitions to the QVH or QAH states when a magnetic field is applied. Furthermore, the QVH and QAH states can be interchanged by tilting the magnetic field.

In Fig. 1, the state with the lowest energy is summarized as a function of both in-plane and out-of-plane components $(B_\parallel, B_\perp)$. The sole undetermined parameter in the figure is the critical field B_C, which is defined such that the product $B_C \times M_{\text{orb}}^{z(\text{QAH})}$ equals the magnetostatic energy of the QAH state. Additionally, some boundaries are characterized by valley flips, representing first-order transitions. Resulting hysteresis scans of the Hall conductance is discussed in Appendix D.

V. INTERLOCKING STRUCTURE IN CHARGE DENSITY

While the focus has been on the QAH, QSH, and QVH states, it is important to consider other competitive states.

Figure 4(a) depicts the HF band structure of a metastable solution at $\nu = 2$. The difference in many-body energy from the lowest energy state, as shown in Fig. 2(a), is about 0.00015 eV per particle. Although both band structures appear quite similar, one band in Fig. 4(a) has a zero band Chern number.

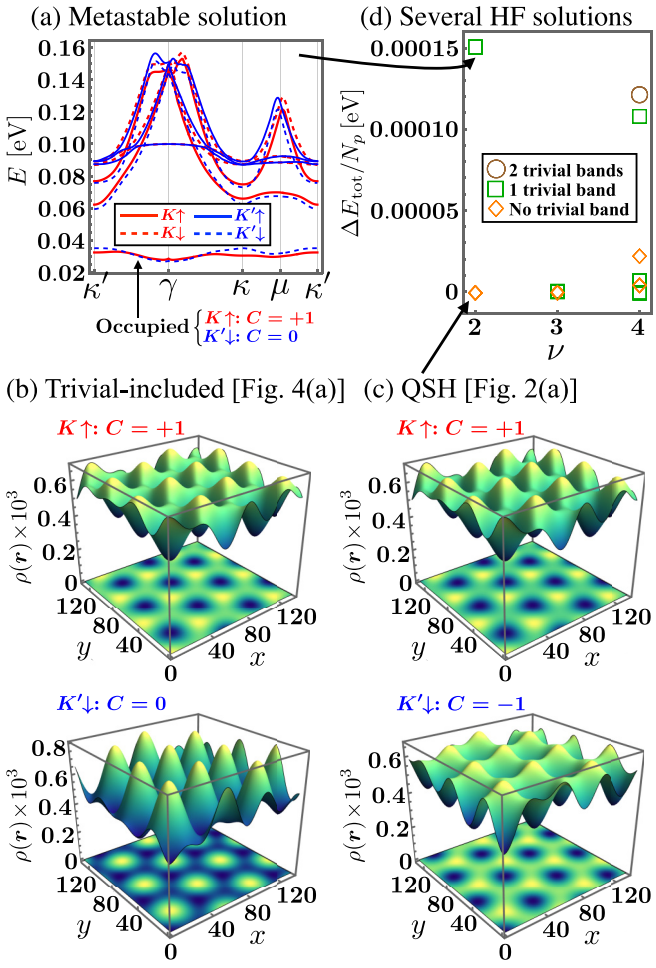

FIG. 4. (a) Hartree-Fock (HF) band structure for a metastable solution at $\nu = 2$, where one of the two lowest bands is characterized by $C = 0$. (b), (c) Charge density $\rho(\boldsymbol{r})$, where the position $\boldsymbol{r} = (x, y)$ is scaled by the lattice constant of graphene $a_{\rm G}$. (b) and (c) correspond to the charge densities for the two lowest bands depicted in Figs. 2(a) and 4(a), respectively. Bands with $|C| = 1$ exhibit an extended structure, while that with $C = 0$ displays localized densities. Light and dark colors indicate areas of high and low density, respectively. (d) HF calculations were performed with 10-20 randomized initial states. This panel plots the difference in many-body energy per particle relative to the lowest value at each ν. (There seem to be a few plots because of the degeneracy). The color of the plots denotes the number of trivial bands.

The two lowest bands in Fig. 4(a) exhibit density structures with an interlocking pattern. While the densities of the topologically trivial and nontrivial bands are qualitatively similar, the trivial band exhibits slightly more localized structure. Each localized density in the trivial band fits into a low-density area of the Chern band. For comparison, Fig. 4(c) plots $\rho(\boldsymbol{r})$ of the QSH state from Fig. 2(a), where the two Chern bands also show interlocking patterns but slightly more extended structures. Despite the seemingly more stable interlocking shape in Fig. 4(b), the trivial-included state is not the lowest energy state. This indicates that forming the trivial band requires more energy than the advantage gained from the interlocking structure.

TABLE II. Spin and orbital magnetizations, $M_{\rm spin}$ and $M^z_{\rm orb}$, for the low-energy states depicted in Fig. 4(d). Both magnetizations are quantified in units of $2\mu_B n_e$.

ν	Type	$\Delta E_{\rm tot}/N_p$ [eV]	$M_{\rm spin}$	$\lvert M^z_{\rm orb}\rvert$
3	$\mathrm{PH}_{\nu=1}$	0	1/3	1.5
	trivial ⊗ QAH	$\lesssim 10^{-6}$	1/3	2.8
	trivial ⊗ QSH		1/3	0.3
	trivial ⊗ QVH		1/3	0.3
4	trivial ⊗ $\mathrm{PH}_{\nu=1}$	0	0	0.9
	$\mathrm{PH}_{\nu=0}$	$5.\times 10^{-6}$	0	0.0

VI. LOWEST ENERGY STATES AT $\nu = 3$ AND 4

Using the analogy at $\nu = 2$, one might anticipate that the ground states at $\nu = 3$ and 4 would exclusively involve the Chern bands. (Associating them with the particle-hole-like counterparts of the $\nu = 1$ and 0 ground states within the Chern band subspace, we call them $\mathrm{PH}_{\nu=1}$ and $\mathrm{PH}_{\nu=0}$ states, respectively). However, our findings indicate that this expectation does not always hold; the trivial-included states may achieve the lowest energy.

In Fig. 4(d), we present HF calculations for $\nu = 2, 3, 4$ using 10-20 randomized initial states and plot the many-body energy differences relative to the lowest observed value per particle, denoted by $\Delta E_{\rm tot}/N_p$. The color coding in the plots indicates the number of occupied trivial bands. The ground state at $\nu = 3$ does not feature a trivial band and corresponds to the $\mathrm{PH}_{\nu=1}$ state, yet the energy difference between this state and the trivial-included state is significantly smaller compared to that at $\nu = 2$. Crucially, at $\nu = 4$, the ground state includes the trivial band.

These results suggest that with increasing ν, the intricate structures in the electron densities become increasingly favorable, rendering the trivial-included state at $\nu = 4$ energetically more advantageous than the $\mathrm{PH}_{\nu=0}$ state. The band structures and electron densities at $\nu = 3$ and 4 are presented in Appendix E.

Before concluding, let us examine the phases observed at filling factors $\nu = 3$ and 4 under different conditions of magnetic fields. Table II presents the spin and orbital magnetizations of the low-energy states depicted in Fig. 4(d). At both $\nu = 3$ and 4, the ground state of the HF Hamiltonian ($\Delta E_{\rm tot} = 0$) exhibits finite magnetization. Conversely, states with the smallest magnetization (i.e., the lowest magnetostatic energy) possess a finite $\Delta E_{\rm tot}$. Therefore, either state can be the lowest energy states in the absence of a magnetic field, depending on the ratio of $\Delta E_{\rm tot}$ to the magnetostatic energy. Upon application of an out-of-plane magnetic field of sufficient amplitude, the system transitions to the state with the largest $|M^z_{\rm orb}|$, specifically the trivial ⊗ QAH (trivial ⊗ $\mathrm{PH}_{\nu=1}$) state at $\nu = 3$ (4).

VII. CONCLUDING REMARKS

This study demonstrated the interplay arising as a result of many-body effects among three topologically distinct states–the QAH, QSH, and QVH states–in pentalayer rhombohedral

graphene on hBN at $\nu = 2$. In the absence of a magnetic field, the QSH phase, characterized by zero magnetization, is predominant due to minimal magnetostatic energy. Application of in-plane or out-of-plane magnetic fields, however, shifts the preference towards the QVH and QAH states, respectively. Therefore, manipulation of these states can be controlled by applying and orienting a magnetic field accordingly. In this work, we ignore the effects of sublattice asymmetric short-range electron-electron and electron-phonon interactions [89–91]. It is tempting to ask how these interactions lift the degeneracies of the QAH, QSH, and QVH states. Additionally, we have demonstrated that the inclusion of the trivial state facilitates the formation of the lowest energy state at $\nu = 3$ and 4. This allows for the emergence of multiple topological phases.

Recent propositions suggest that composite fermions (CFs) [92,93] form in twisted bilayer $MoTe_2$ even in the absence of an external magnetic field [25,26]. Generally, the CF theory establishes a mapping between the multicomponent fractional and integer quantum Hall effects [93–95]. If the CF picture holds valid in pentalayer rhombohedral graphene on hBN, our findings might significantly advance the understanding of fractional QAH physics.

ACKNOWLEDGMENTS

We acknowledge the computational resources offered by Research Institute for Information Technology, Kyushu University. The work is supported in part by JSPS KAKENHI Grants No. JP23K19036, No. JP24K06926, and No. JP20H01830, and JST CREST Grant No. JPMJCR18T2.

APPENDIX A: PENTALAYER RHOMBOHEDRAL GRAPHENE

The tight-binding Hamiltonian of pentalayer rhombohedral graphene is given by [31,33,82,96]

$$\tilde{h}_{\mathrm{R5G}}(\boldsymbol{k}) = \begin{pmatrix} D_1 & V & W & 0 & 0 \\ V^\dagger & D_2 & V & W & 0 \\ W^\dagger & V^\dagger & D_3 & V & W \\ 0 & W^\dagger & V^\dagger & D_4 & V \\ 0 & 0 & W^\dagger & V^\dagger & D_5 \end{pmatrix} \tag{A1}$$

where

$$D_l = \begin{pmatrix} 0 & t_0 g(\boldsymbol{k}) \\ t_0 g^*(\boldsymbol{k}) & 0 \end{pmatrix} + u_D(l-3), \tag{A2}$$

$$V = \begin{pmatrix} t_4 g^*(\boldsymbol{k}) & t_1 \\ t_3 g(\boldsymbol{k}) & t_4 g^*(\boldsymbol{k}) \end{pmatrix}, \tag{A3}$$

$$W = \begin{pmatrix} 0 & 0 \\ t_2 & 0 \end{pmatrix}, \tag{A4}$$

$$g(\boldsymbol{k}) = \sum_{i=1}^{3} e^{-i\boldsymbol{k}\cdot\tau_i}. \tag{A5}$$

Here, t_0 and (t_1, t_2, t_3, t_4) are the intralayer and interlayer hopping terms (see Fig. 5), u_D is the interlayer potential difference induced by a perpendicular displacement field, and τ_i's are the vectors connecting the nearest neighbor sublattices. The effective continuum Hamiltonian

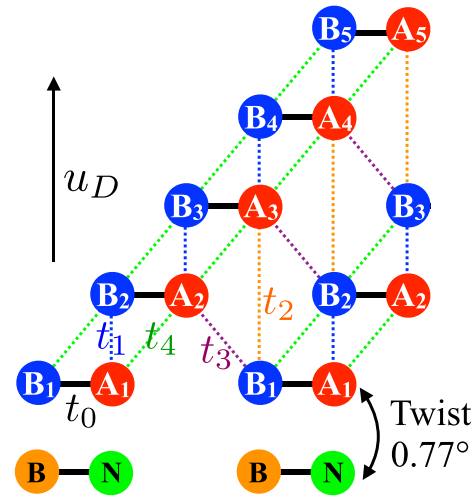

FIG. 5. Pentalayer rhombohedral graphene on hBN layer. A_l and B_l are the sublattices of the lth layer. The solid and dotted lines represent intralayer t_0 and interlayer (t_1, t_2, t_3, t_4) hopping terms. The twist angle between graphene and hBN is 0.77°. A perpendicular displacement field induces the interlayer potential difference u_D.

$h_{\mathrm{R5G}}(\boldsymbol{k})$ in the main text is given by replacing $g(\boldsymbol{k})$ with $a_{\mathrm{G}}\sqrt{3}/2(\xi k_x - ik_y)$, where a_{G} is the lattice constant of graphene and $\xi = +1$ (-1) for the valley K (K'). Each parameter in Fig. 5 is assigned as $(t_0, t_1, t_2, t_3, t_4, u_D) = (-3100, 380, -10.5, 290, 141, 50)$ meV, expected to match experimental conditions for the $\nu = 1$ QAH effect [5,31,33,82].

APPENDIX B: MOIRÉ POTENTIAL

We describe an effective continuum model for a moiré potential, following an approach in Ref. [60]. Now, we consider the bottom layer of pentalayer rhombohedral graphene and hBN. The lattice constants of graphene and hBN are fixed as $a_{\mathrm{G}} = 0.246$ nm and $a_{\mathrm{hBN}} = 0.2504$ nm [97], inducing the lattice mismatch as $\epsilon = a_{\mathrm{hBN}}/a_{\mathrm{G}} - 1 \approx 1.8\%$. The twist angle is set to $\theta = 0.77°$ to align with the experiment in Ref. [5].

Let us first derive the primitive vectors of the moiré superlattice and the corresponding reciprocal lattice vectors. We denote the primitive lattice vectors of graphene by $\boldsymbol{a}_i$ with $i = 1, 2$. For hBN, we have

$$\tilde{\boldsymbol{a}}_i = MR\boldsymbol{a}_i, \tag{B1}$$

where $M = (1+\epsilon)\mathbf{1}$, and R is a rotation matrix by θ. This relation implies that a lattice of hBN at $\boldsymbol{r}$ has its counterpart of graphene at $R^{-1}M^{-1}\boldsymbol{r}$. Their displacement is

$$\boldsymbol{\delta}(\boldsymbol{r}) = (1 - R^{-1}M^{-1})\boldsymbol{r}. \tag{B2}$$

The primitive vectors of the moiré superlattice $\boldsymbol{L}_i^{\mathrm{M}}$ is defined so that $\boldsymbol{\delta}(\boldsymbol{L}_i^{\mathrm{M}}) = \boldsymbol{a}_i$:

$$\boldsymbol{L}_i^{\mathrm{M}} = (1 - R^{-1}M^{-1})^{-1}\boldsymbol{a}_i. \tag{B3}$$

In our settings, we have $|\boldsymbol{L}_i^{\mathrm{M}}| \approx 45.4 a_{\mathrm{G}} \approx 11.2$nm. The moiré reciprocal lattice vectors, satisfying $\boldsymbol{L}_i^{\mathrm{M}} \cdot \boldsymbol{G}_i^{\mathrm{M}} = 2\pi\delta_{ij}$, are given by

$$\boldsymbol{G}_i^{\mathrm{M}} = (1 - M^{-1}R)\boldsymbol{a}_i^* = \boldsymbol{a}_i^* - \tilde{\boldsymbol{a}}_i^*, \tag{B4}$$

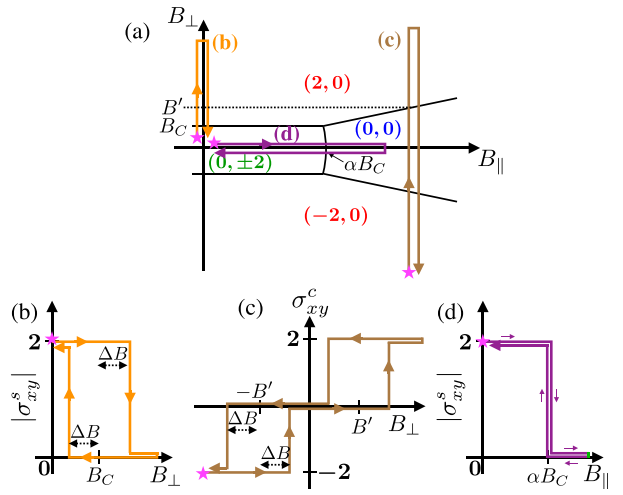

FIG. 6. (a) The same as Fig. 1. The three paths under consideration are illustrated, labeled by subsequent panels. The charge and spin Chern numbers (C_c, C_s) for each region are highlighted in red for QAH, green for QSH, and blue for QVH states. The magenta stars indicate the initial points of each path. (b)–(d) Charge and spin Hall conductances σ^c_{xy} and $|\sigma^s_{xy}|$. The coercive field in (b),(c) is represented by ΔB.

where $\boldsymbol{a}_i^*$ and $\tilde{\boldsymbol{a}}_i^*$ are the reciprocal lattice vectors of graphene and hBN, satisfying $\boldsymbol{a}_i \cdot \boldsymbol{a}_j^* = \tilde{\boldsymbol{a}}_i \cdot \tilde{\boldsymbol{a}}_j^* = 2\pi\delta_{ij}$. Here, the relation $\tilde{\boldsymbol{a}}_i^* = M^{-1}R\boldsymbol{a}_i^*$ is obtained by $\boldsymbol{a}_i \cdot \boldsymbol{a}_j^* = \boldsymbol{a}_i^T \boldsymbol{a}_j^* = (R^{-1}M^{-1}\tilde{\boldsymbol{a}}_i)^T \boldsymbol{a}_j^* = \tilde{\boldsymbol{a}}_i^T M^{-1}R\boldsymbol{a}_j^*$.

The bilayer system composed of graphene and hBN is effectively described by a tight-binding lattice Hamiltonian. Eliminating the hBN bases based on the second order perturbation within an effective continuum framework, the effect of the hBN (for a given valley and spin) is represented by a local potential $v(\boldsymbol{r})$ within the graphene subspace [60]:

$$v(\boldsymbol{r}) = V_0 \begin{pmatrix} 1 & 0 \\ 0 & 1 \end{pmatrix} + \left\{ V_1 e^{i\xi\psi} \left[\begin{pmatrix} 1 & \omega^{-\xi} \\ 1 & \omega^{-\xi} \end{pmatrix} e^{i\xi \boldsymbol{G}_1^{\mathrm{M}} \cdot \boldsymbol{r}} + \begin{pmatrix} 1 & \omega^{\xi} \\ \omega^{\xi} & \omega^{-\xi} \end{pmatrix} e^{i\xi \boldsymbol{G}_2^{\mathrm{M}} \cdot \boldsymbol{r}} + \begin{pmatrix} 1 & 1 \\ \omega^{-\xi} & \omega^{-\xi} \end{pmatrix} e^{-i\xi \left(\boldsymbol{G}_1^{\mathrm{M}} + \boldsymbol{G}_2^{\mathrm{M}}\right) \cdot \boldsymbol{r}} \right] + \mathrm{H.c.} \right\}, \quad \text{(B5)}$$

where $\omega = \exp\{2\pi i/3\}$ and $\xi = +1$ (-1) for the valley K (K'). Here, we use $V_0 = 28.9\,\mathrm{meV}$, $V_1 = 21.0\,\mathrm{meV}$ and $\psi = -0.29\,\mathrm{rad}$ following Ref. [60]. As mentioned in the main text, its second quantized form is

$$V_{\mathrm{hBN}} = \sum_{\boldsymbol{k}} \sum_{m_1 m_2} \tilde{\boldsymbol{c}}^\dagger(\boldsymbol{k} + m_1\boldsymbol{G}_1 + m_2\boldsymbol{G}_2) v(m_1, m_2) \tilde{\boldsymbol{c}}(\boldsymbol{k}), \quad \text{(B6)}$$

where $\tilde{\boldsymbol{c}}^\dagger = (c^\dagger_{A_1}, c^\dagger_{B_1})$ and $v(m_1, m_2)$ is the Fourier coefficient of $v(\boldsymbol{r})$. In the numerical calculations, the summation $\sum_{\boldsymbol{k}} \sum_{m_1 m_2}$ is confined to the first and second moiré BZs.

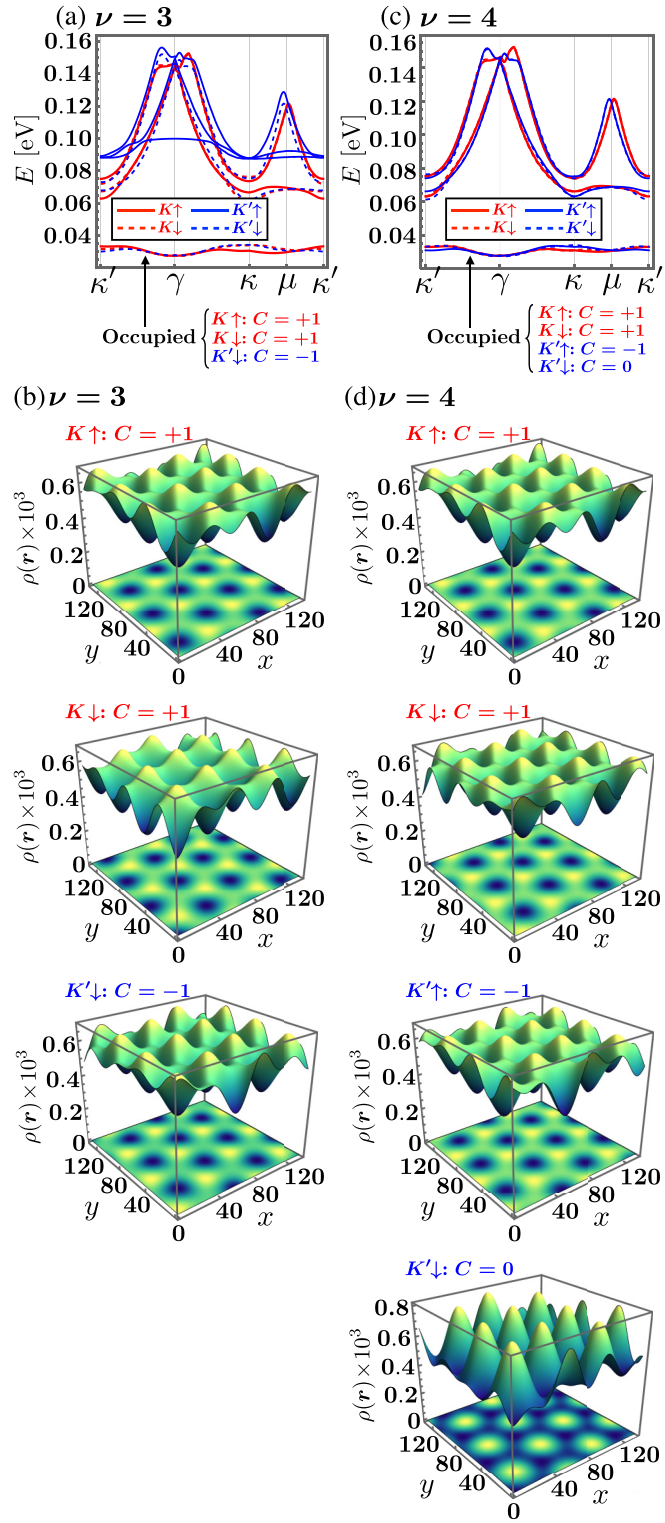

FIG. 7. (a) HF band structure at $\nu = 3$. The three lowest bands carry $C = +1$ or -1. (b) Charge densities $\rho(\boldsymbol{r})$ of the three lowest bands in (a). (c) HF band structure at $\nu = 4$. One of the four lowest bands carries $C = 0$. (d) Charge densities $\rho(\boldsymbol{r})$ of the four lowest bands in (c).

APPENDIX C: HARTREE-FOCK CALCULATION

Let us describe the self-consistent HF calculation. As mentioned in the main text, the interaction before the mean-field approximation has the form of

$$H_{\text{int}} = \frac{1}{2S}\sum_{\boldsymbol{k}\boldsymbol{k}'\boldsymbol{q}}\sum_{ZZ'} V_C(\boldsymbol{q}) c_Z^\dagger(\boldsymbol{k}+\boldsymbol{q}) c_{Z'}^\dagger(\boldsymbol{k}'-\boldsymbol{q}) c_{Z'}(\boldsymbol{k}') c_Z(\boldsymbol{k}), \tag{C1}$$

where S is the area of the system, and Z and Z' represent the spin, valley, sublattice and layer indices. Here, we set the positions of both K and K' to be the center in the folded moiré BZ for simplicity. The form of $V_C(\boldsymbol{q})$ is written in the main text. We then construct the Hartree and Fock Hamiltonians as

$$H_{\text{H}} = \frac{1}{S}\sum_{\boldsymbol{k}\boldsymbol{k}'\boldsymbol{q}}\sum_{ZZ'} V_C(\boldsymbol{q}) \langle c_{Z'}^\dagger(\boldsymbol{k}'-\boldsymbol{q}) c_{Z'}(\boldsymbol{k}')\rangle c_Z^\dagger(\boldsymbol{k}+\boldsymbol{q}) c_Z(\boldsymbol{k}), \tag{C2}$$

$$H_{\text{F}} = -\frac{1}{S}\sum_{\boldsymbol{k}\boldsymbol{k}'\boldsymbol{q}}\sum_{ZZ'} V_C(\boldsymbol{q}) \langle c_{Z'}^\dagger(\boldsymbol{k}'-\boldsymbol{q}) c_Z(\boldsymbol{k})\rangle c_Z^\dagger(\boldsymbol{k}+\boldsymbol{q}) c_{Z'}(\boldsymbol{k}'), \tag{C3}$$

where $\langle\cdot\rangle$ represents the expectation value for the ground state. Now, we pick up terms that couple momenta modulo the moiré reciprocal lattice vectors. In other words, using a set of reciprocal lattice vectors of the moiré superlattice, denoted $\boldsymbol{G}$, we add constraints $\boldsymbol{k}+\boldsymbol{q} = \boldsymbol{k}+\boldsymbol{G}$ and $\boldsymbol{k}+\boldsymbol{q} = \boldsymbol{k}'+\boldsymbol{G}$ in Eqs. (C2) and (C3), respectively:

$$H_{\text{H}} \to \frac{1}{S}\sum_{\boldsymbol{k}\boldsymbol{k}'\boldsymbol{G}}\sum_{ZZ'} V_C(\boldsymbol{G}) \langle c_{Z'}^\dagger(\boldsymbol{k}'-\boldsymbol{G}) c_{Z'}(\boldsymbol{k}')\rangle c_Z^\dagger(\boldsymbol{k}+\boldsymbol{G}) c_Z(\boldsymbol{k}), \tag{C4}$$

$$H_{\text{F}} \to -\frac{1}{S}\sum_{\boldsymbol{k}\boldsymbol{k}'\boldsymbol{G}}\sum_{ZZ'} V_C(\boldsymbol{k}'-\boldsymbol{k}+\boldsymbol{G}) \langle c_{Z'}^\dagger(\boldsymbol{k}-\boldsymbol{G}) c_Z(\boldsymbol{k})\rangle \times c_Z^\dagger(\boldsymbol{k}'+\boldsymbol{G}) c_{Z'}(\boldsymbol{k}'). \tag{C5}$$

In the numerical calculation, the summation $\sum_{\boldsymbol{k}\boldsymbol{k}'\boldsymbol{G}}$ is confined to the first and second moiré BZs. When seeking the ground state of the HF Hamiltonian for given system parameters, we perform the self-consistent calculations with 10−20 randomized initial states. Specifically, we plug random numbers into $\langle c_{Z'}^\dagger(\boldsymbol{k}') c_Z(\boldsymbol{k})\rangle$ in the HF Hamiltonian and solve them self-consistently.

APPENDIX D: HYSTERESIS

We discuss hysteresis scans of the charge and spin Hall conductances σ_{xy}^c and σ_{xy}^s. We consider three paths in the $(B_\perp, B_\parallel)$ space as illustrated in Fig. 6(a). (In the QSH region of the figure, the spin Chern number C_s is denoted as ± 2 to reflects the degeneracy of the states #3 and #4 in Table I. Although either state should be favored due to weak spin-orbit interactions in real systems, we simplify our argument by considering only $|\sigma_{xy}^s|$ below. Note that the QSH state we consider carries nonzero valley Chern number as well [81]).

Figures 6(b)–6(d) depicts anticipated behaviors of the Hall conductance. Figures 6(b) and 6(c) exhibit hysteresis since transitions from the QAH to QSH/QVH states involve valley flips, leading to a first-order transition. The coercive field ΔB in both figures is expected to be comparable to the experimentally observed one for the $\nu = 1$ QAH effect [5] because the valley of only one band needs to be flipped. Conversely, Fig. 6(d) shows no hysteresis behavior since transition from the QSH to QVH states involves only spin flips. The SU(2) spin-rotational symmetry prevents hysteresis behavior in such cases.

APPENDIX E: NUMERICAL RESULTS AT $\nu = 3$ AND 4

Let us discuss the HF band structures and charge densities at $\nu = 3$ and 4. Figure 7(a) presents the band structure of the lowest energy state at $\nu = 3$. The occupied three lowest bands are separated from other conduction bands. Each band carries the Chern number $C = +1$ or -1 depending on the valley. Their charge densities $\rho(\boldsymbol{r})$ are shown in Fig. 7(b). They provide similar (but shifted) extended structure.

Figure 7(c) presents the band structure of the lowest energy state at $\nu = 4$. The occupied four lowest bands are separated from other conduction bands. Three bands carry $C = +1$ or -1 while the other does $C = 0$. Their charge densities are shown in Fig. 7(d).

[1] J. Cai, E. Anderson, C. Wang, X. Zhang, X. Liu, W. Holtzmann, Y. Zhang, F. Fan, T. Taniguchi, K. Watanabe, Y. Ran, T. Cao, L. Fu, D. Xiao, W. Yao, and X. Xu, Signatures of fractional quantum anomalous Hall states in twisted $MoTe_2$, Nature (London) **622**, 63 (2023).

[2] Y. Zeng, Z. Xia, K. Kang, J. Zhu, P. Knüppel, C. Vaswani, K. Watanabe, T. Taniguchi, K. F. Mak, and J. Shan, Thermodynamic evidence of fractional Chern insulator in moiré $MoTe_2$, Nature (London) **622**, 69 (2023).

[3] H. Park, J. Cai, E. Anderson, Y. Zhang, J. Zhu, X. Liu, C. Wang, W. Holtzmann, C. Hu, Z. Liu, T. Taniguchi, K. Watanabe, J.-H. Chu, T. Cao, L. Fu, W. Yao, C.-Z. Chang, D. Cobden, D. Xiao, and X. Xu, Observation of fractionally quantized anomalous Hall effect, Nature (London) **622**, 74 (2023).

[4] F. Xu, Z. Sun, T. Jia, C. Liu, C. Xu, C. Li, Y. Gu, K. Watanabe, T. Taniguchi, B. Tong, J. Jia, Z. Shi, S. Jiang, Y. Zhang, X. Liu, and T. Li, Observation of integer and fractional quantum anomalous Hall effects in twisted bilayer $MoTe_2$, Phys. Rev. X **13**, 031037 (2023).

[5] Z. Lu, T. Han, Y. Yao, A. P. Reddy, J. Yang, J. Seo, K. Watanabe, T. Taniguchi, L. Fu, and L. Ju, Fractional quantum anomalous Hall effect in multilayer graphene, Nature (London) **626**, 759 (2024).

[6] E. Y. Andrei and A. H. MacDonald, Graphene bilayers with a twist, Nat. Mater. **19**, 1265 (2020).

[7] K. F. Mak and J. Shan, Semiconductor moiré materials, Nat. Nanotechnol. **17**, 686 (2022).

[8] Y. Cao, V. Fatemi, S. Fang, K. Watanabe, T. Taniguchi, E. Kaxiras, and P. Jarillo-Herrero, Unconventional superconduc-

tivity in magic-angle graphene superlattices, Nature (London) **556**, 43 (2018).

[9] A. L. Sharpe, E. J. Fox, A. W. Barnard, J. Finney, K. Watanabe, T. Taniguchi, M. A. Kastner, and D. Goldhaber-Gordon, Emergent ferromagnetism near three-quarters filling in twisted bilayer graphene, Science **365**, 605 (2019).

[10] H. Li, S. Li, E. C. Regan, D. Wang, W. Zhao, S. Kahn, K. Yumigeta, M. Blei, T. Taniguchi, K. Watanabe, S. Tongay, A. Zettl, M. F. Crommie, and F. Wang, Imaging two-dimensional generalized Wigner crystals, Nature (London) **597**, 650 (2021).

[11] C. Jin, Z. Tao, T. Li, Y. Xu, Y. Tang, J. Zhu, S. Liu, K. Watanabe, T. Taniguchi, J. C. Hone, L. Fu, J. Shan, and K. F. Mak, Stripe phases in WSe_2/WS_2 moiré superlattices, Nat. Mater. **20**, 940 (2021).

[12] E. Anderson, F.-R. Fan, J. Cai, W. Holtzmann, T. Taniguchi, K. Watanabe, D. Xiao, W. Yao, and X. Xu, Programming correlated magnetic states with gate-controlled moiré, Science **381**, 325 (2023).

[13] C. R. Dean, L. Wang, P. Maher, C. Forsythe, F. Ghahari, Y. Gao, J. Katoch, M. Ishigami, P. Moon, M. Koshino, T. Taniguchi, K. Watanabe, K. L. Shepard, J. Hone, and P. Kim, Hofstadter's butterfly and the fractal quantum Hall effect in moiré superlattices, Nature (London) **497**, 598 (2013).

[14] E. M. Spanton, A. A. Zibrov, H. Zhou, T. Taniguchi, K. Watanabe, M. P. Zaletel, and A. F. Young, Observation of fractional Chern insulators in a van der Waals heterostructure, Science **360**, 62 (2018).

[15] J. Liu, Z. Ma, J. Gao, and X. Dai, Quantum valley Hall effect, orbital magnetism, and anomalous Hall effect in twisted multilayer graphene systems, Phys. Rev. X **9**, 031021 (2019).

[16] K. Kang, B. Shen, Y. Qiu, Y. Zeng, Z. Xia, K. Watanabe, T. Taniguchi, J. Shan, and K. F. Mak, Evidence of the fractional quantum spin Hall effect in moiré $MoTe_2$, Nature (London) **628**, 522 (2024).

[17] K. Kang, Y. Qiu, K. Watanabe, T. Taniguchi, J. Shan, and K. F. Mak, Double quantum spin Hall phase in moiré WSe_2, Nano Lett. **24**, 14901 (2024).

[18] Z. Liu and E. J. Bergholtz, Recent developments in fractional Chern insulators, in *Encyclopedia of Condensed Matter Physics (Second Edition)*, edited by T. Chakraborty (Academic, Oxford, 2024), pp. 515–538.

[19] M. Serlin, C. L. Tschirhart, H. Polshyn, Y. Zhang, J. Zhu, K. Watanabe, T. Taniguchi, L. Balents, and A. F. Young, Intrinsic quantized anomalous Hall effect in a moiré heterostructure, Science **367**, 900 (2020).

[20] Y. Deng, Y. Yu, M. Z. Shi, Z. Guo, Z. Xu, J. Wang, X. H. Chen, and Y. Zhang, Quantum anomalous Hall effect in intrinsic magnetic topological insulator $MnBi_2Te_4$, Science **367**, 895 (2020).

[21] T. Li, S. Jiang, B. Shen, Y. Zhang, L. Li, Z. Tao, T. Devakul, K. Watanabe, T. Taniguchi, L. Fu, J. Shan, and K. F. Mak, Quantum anomalous Hall effect from intertwined moiré bands, Nature (London) **600**, 641 (2021).

[22] B. A. Foutty, C. R. Kometter, T. Devakul, A. P. Reddy, K. Watanabe, T. Taniguchi, L. Fu, and B. E. Feldman, Mapping twist-tuned multiband topology in bilayer WSe_2, Science **384**, 343 (2024).

[23] A. P. Reddy, F. Alsallom, Y. Zhang, T. Devakul, and L. Fu, Fractional quantum anomalous Hall states in twisted bilayer $MoTe_2$ and WSe_2, Phys. Rev. B **108**, 085117 (2023).

[24] C. Wang, X.-W. Zhang, X. Liu, Y. He, X. Xu, Y. Ran, T. Cao, and D. Xiao, Fractional Chern insulator in twisted bilayer $MoTe_2$, Phys. Rev. Lett. **132**, 036501 (2024).

[25] J. Dong, J. Wang, P. J. Ledwith, A. Vishwanath, and D. E. Parker, Composite Fermi liquid at zero magnetic field in twisted $MoTe_2$, Phys. Rev. Lett. **131**, 136502 (2023).

[26] H. Goldman, A. P. Reddy, N. Paul, and L. Fu, Zero-field composite Fermi liquid in twisted semiconductor bilayers, Phys. Rev. Lett. **131**, 136501 (2023).

[27] A. P. Reddy and L. Fu, Toward a global phase diagram of the fractional quantum anomalous Hall effect, Phys. Rev. B **108**, 245159 (2023).

[28] C. Xu, J. Li, Y. Xu, Z. Bi, and Y. Zhang, Maximally localized Wannier functions, interaction models, and fractional quantum anomalous Hall effect in twisted bilayer $MoTe_2$, Proc. Natl. Acad. Sci. USA **121**, e2316749121 (2024).

[29] T. Wang, T. Devakul, M. P. Zaletel, and L. Fu, Diverse magnetic orders and quantum anomalous Hall effect in twisted bilayer $MoTe_2$ and WSe_2, arXiv:2306.02501.

[30] J. Yu, J. Herzog-Arbeitman, M. Wang, O. Vafek, B. A. Bernevig, and N. Regnault, Fractional Chern insulators versus non-magnetic states in twisted bilayer $MoTe_2$, Phys. Rev. B **109**, 045147 (2023).

[31] Z. Dong, A. S. Patri, and T. Senthil, Theory of fractional quantum anomalous Hall phases in pentalayer rhombohedral graphene moiré structures, Phys. Rev. Lett. **133**, 206502 (2024).

[32] B. Zhou, H. Yang, and Y.-H. Zhang, Fractional quantum anomalous Hall effects in rhombohedral multilayer graphene in the moiréless limit, Phys. Rev. Lett. **133**, 206504 (2024).

[33] J. Dong, T. Wang, T. Wang, T. Soejima, M. P. Zaletel, A. Vishwanath, and D. E. Parker, Anomalous Hall crystals in rhombohedral multilayer graphene I: Interaction-driven Chern bands and fractional quantum Hall states at zero magnetic field, Phys. Rev. Lett. **133**, 206503 (2024).

[34] Z. Guo, X. Lu, B. Xie, and J. Liu, Fractional Chern insulator states in multilayer graphene moir superlattices, Phys. Rev. B **110**, 075109 (2024).

[35] Y. H. Kwan, J. Yu, J. Herzog-Arbeitman, D. K. Efetov, N. Regnault, and B. A. Bernevig, Moiré fractional Chern insulators III: Hartree-Fock phase diagram, magic angle regime for Chern insulator states, the role of the moiré potential and goldstone gaps in rhombohedral graphene superlattices, arXiv:2312.11617.

[36] J. Herzog-Arbeitman, Y. Wang, J. Liu, P. M. Tam, Z. Qi, Y. Jia, D. K. Efetov, O. Vafek, N. Regnault, H. Weng, Q. Wu, B. A. Bernevig, and J. Yu, Moiré fractional Chern insulators. II. First-principles calculations and continuum models of rhombohedral graphene superlattices, Phys. Rev. B **109**, 205122 (2024).

[37] Z. Liu and J. Wang, Layer-dependent quantum anomalous Hall effect in rhombohedral graphene, arXiv:2401.13413.

[38] Y. Zeng, D. Guerci, V. Crpel, A. J. Millis, and J. Cano, Sublattice structure and topology in spontaneously crystallized electronic states, Phys. Rev. Lett. **132**, 236601 (2024).

[39] T. Tan and T. Devakul, Parent Berry curvature and the ideal anomalous Hall crystal, Phys. Rev. X **14**, 041040 (2024).

[40] T. Soejima, J. Dong, T. Wang, T. Wang, M. P. Zaletel, A. Vishwanath, and D. E. Parker, Anomalous Hall crystals in rhombohedral multilayer graphene II: General mechanism and a minimal model, Phys. Rev. B **110**, 205124 (2024).

[41] Z. Dong, A. S. Patri, and T. Senthil, Stability of anomalous Hall crystals in multilayer rhombohedral graphene, Phys. Rev. B **110**, 205130 (2024).
[42] M. Xie and S. D. Sarma, Integer and fractional quantum anomalous Hall effects in pentalayer graphene, Phys. Rev. B **109**, L241115 (2024).
[43] D. N. Sheng, A. P. Reddy, A. Abouelkomsan, E. J. Bergholtz, and L. Fu, Quantum anomalous Hall crystal at fractional filling of moiré superlattices, Phys. Rev. Lett. **133**, 066601 (2024).
[44] H. Lu, H.-Q. Wu, B.-B. Chen, and Z. Y. Meng, Direct transition from a fractional quantum anomalous Hall state to a smectic state with the same Hall conductance, arXiv:2404.06745.
[45] K. P. Nuckolls and A. Yazdani, A microscopic perspective on moiré materials, Nat. Rev. Mater. **9**, 460 (2024).
[46] F. Zhang, J. Jung, G. A. Fiete, Q. Niu, and A. H. MacDonald, Spontaneous quantum Hall states in chirally stacked few-layer graphene systems, Phys. Rev. Lett. **106**, 156801 (2011).
[47] H. Zhou, T. Xie, A. Ghazaryan, T. Holder, J. R. Ehrets, E. M. Spanton, T. Taniguchi, K. Watanabe, E. Berg, M. Serbyn, and A. F. Young, Half- and quarter-metals in rhombohedral trilayer graphene, Nature (London) **598**, 429 (2021).
[48] H. Zhou, T. Xie, T. Taniguchi, K. Watanabe, and A. F. Young, Superconductivity in rhombohedral trilayer graphene, Nature (London) **598**, 434 (2021).
[49] H. Zhou, L. Holleis, Y. Saito, L. Cohen, W. Huynh, C. L. Patterson, F. Yang, T. Taniguchi, K. Watanabe, and A. F. Young, Isospin magnetism and spin-polarized superconductivity in Bernal bilayer graphene, Science **375**, 774 (2022).
[50] S. C. de la Barrera, S. Aronson, Z. Zheng, K. Watanabe, T. Taniguchi, Q. Ma, P. Jarillo-Herrero, and R. Ashoori, Cascade of isospin phase transitions in Bernal-stacked bilayer graphene at zero magnetic field, Nat. Phys. **18**, 771 (2022).
[51] Y. Zhang, R. Polski, A. Thomson, É. Lantagne-Hurtubise, C. Lewandowski, H. Zhou, K. Watanabe, T. Taniguchi, J. Alicea, and S. Nadj-Perge, Enhanced superconductivity in spin–orbit proximitized bilayer graphene, Nature (London) **613**, 268 (2023).
[52] T. Han, Z. Lu, G. Scuri, J. Sung, J. Wang, T. Han, K. Watanabe, T. Taniguchi, L. Fu, H. Park, and L. Ju, Orbital multiferroicity in pentalayer rhombohedral graphene, Nature (London) **623**, 41 (2023).
[53] T. Han, Z. Lu, G. Scuri, J. Sung, J. Wang, T. Han, K. Watanabe, T. Taniguchi, H. Park, and L. Ju, Correlated insulator and Chern insulators in pentalayer rhombohedral-stacked graphene, Nat. Nanotechnol. **19**, 181 (2024).
[54] K. Liu, J. Zheng, Y. Sha, B. Lyu, F. Li, Y. Park, Y. Ren, K. Watanabe, T. Taniguchi, J. Jia, W. Luo, Z. Shi, J. Jung, and G. Chen, Interaction-driven spontaneous broken-symmetry insulator and metals in ABCA tetralayer graphene, arXiv:2306.11042.
[55] M. Das and C. Huang, Superpolarized electron-hole liquid and multiferroicity in multilayer graphene, arXiv:2404.10069.
[56] T. Han, Z. Lu, Y. Yao, J. Yang, J. Seo, C. Yoon, K. Watanabe, T. Taniguchi, L. Fu, F. Zhang, and L. Ju, Large quantum anomalous Hall effect in spin-orbit proximitized rhombohedral graphene, Science **384**, 647 (2024).
[57] L. B. Braz, T. Nag, and A. M. Black-Schaffer, Competing magnetic states on the surface of multilayer ABC-stacked graphene, Phys. Rev. B **110**, L241401 (2024).
[58] J. Xie, Z. Huo, X. Lu, Z. Feng, Z. Zhang, W. Wang, Q. Yang, K. Watanabe, T. Taniguchi, K. Liu, Z. Song, X. C. Xie, J. Liu, and X. Lu, Even- and odd-denominator fractional quantum anomalous Hall effect in graphene moire superlattices, arXiv:2405.16944.
[59] F. Guinea, A. H. Castro Neto, and N. M. R. Peres, Electronic states and Landau levels in graphene stacks, Phys. Rev. B **73**, 245426 (2006).
[60] P. Moon and M. Koshino, Electronic properties of graphene/hexagonal-boron-nitride moiré superlattice, Phys. Rev. B **90**, 155406 (2014).
[61] J. Jung, A. Raoux, Z. Qiao, and A. H. MacDonald, *Ab initio* theory of moiré superlattice bands in layered two-dimensional materials, Phys. Rev. B **89**, 205414 (2014).
[62] K. v. Klitzing, G. Dorda, and M. Pepper, New method for high-accuracy determination of the fine-structure constant based on quantized Hall resistance, Phys. Rev. Lett. **45**, 494 (1980).
[63] R. B. Laughlin, Quantized Hall conductivity in two dimensions, Phys. Rev. B **23**, 5632 (1981).
[64] D. J. Thouless, M. Kohmoto, M. P. Nightingale, and M. den Nijs, Quantized Hall conductance in a two-dimensional periodic potential, Phys. Rev. Lett. **49**, 405 (1982).
[65] D. C. Tsui, H. L. Stormer, and A. C. Gossard, Two-dimensional magnetotransport in the extreme quantum limit, Phys. Rev. Lett. **48**, 1559 (1982).
[66] R. B. Laughlin, Anomalous quantum Hall effect: An incompressible quantum fluid with fractionally charged excitations, Phys. Rev. Lett. **50**, 1395 (1983).
[67] A. K. Geim and K. S. Novoselov, The rise of graphene, Nat. Mater. **6**, 183 (2007).
[68] K. S. Novoselov, A. K. Geim, S. V. Morozov, D. Jiang, M. I. Katsnelson, I. V. Grigorieva, S. V. Dubonos, and A. A. Firsov, Two-dimensional gas of massless Dirac fermions in graphene, Nature (London) **438**, 197 (2005).
[69] Y. Zhang, Y.-W. Tan, H. L. Stormer, and P. Kim, Experimental observation of the quantum Hall effect and Berry's phase in graphene, Nature (London) **438**, 201 (2005).
[70] K. Nomura and A. H. MacDonald, Quantum Hall ferromagnetism in graphene, Phys. Rev. Lett. **96**, 256602 (2006).
[71] V. M. Apalkov and T. Chakraborty, Fractional quantum Hall states of Dirac electrons in graphene, Phys. Rev. Lett. **97**, 126801 (2006).
[72] C. Tőke, P. E. Lammert, V. H. Crespi, and J. K. Jain, Fractional quantum Hall effect in graphene, Phys. Rev. B **74**, 235417 (2006).
[73] X. Du, I. Skachko, F. Duerr, A. Luican, and E. Y. Andrei, Fractional quantum Hall effect and insulating phase of Dirac electrons in graphene, Nature (London) **462**, 192 (2009).
[74] K. I. Bolotin, F. Ghahari, M. D. Shulman, H. L. Stormer, and P. Kim, Observation of the fractional quantum Hall effect in graphene, Nature (London) **462**, 196 (2009).
[75] F. D. M. Haldane, Model for a quantum Hall effect without Landau levels: Condensed-matter realization of the "parity anomaly", Phys. Rev. Lett. **61**, 2015 (1988).
[76] T. Neupert, L. Santos, C. Chamon, and C. Mudry, Fractional quantum Hall states at zero magnetic field, Phys. Rev. Lett. **106**, 236804 (2011).
[77] D. N. Sheng, Z.-C. Gu, K. Sun, and L. Sheng, Fractional quantum Hall effect in the absence of Landau levels, Nat. Commun. **2**, 389 (2011).
[78] N. Regnault and B. A. Bernevig, Fractional Chern insulator, Phys. Rev. X **1**, 021014 (2011).

[79] K. Sun, Z. Gu, H. Katsura, and S. Das Sarma, Nearly flatbands with nontrivial topology, Phys. Rev. Lett. **106**, 236803 (2011).

[80] S. Raghu, X.-L. Qi, C. Honerkamp, and S.-C. Zhang, Topological Mott insulators, Phys. Rev. Lett. **100**, 156401 (2008).

[81] S. F. Islam and C. Benjamin, A scheme to realize the quantum spin-valley Hall effect in monolayer graphene, Carbon **110**, 304 (2016).

[82] Y. Park, Y. Kim, B. L. Chittari, and J. Jung, Topological flat bands in rhombohedral tetralayer and multilayer graphene on hexagonal boron nitride moiré superlattices, Phys. Rev. B **108**, 155406 (2023).

[83] Our HF Hamiltonian commutes with the "valley Zeeman term", $H_V(\boldsymbol{k}) = -b_V(\tau_z \otimes \sigma_0)$, where $\tau_z = \pm$ labels the valleys K and K', and σ_0 is the identity matrix acting in the spin space. This addition merely shifts the energy at each sector. Setting b_V to be sufficiently small, we obtain Fig. 2(b). The additional energy shift [$= \pm b_z \times$ (particle number)] is excluded in the figure. In Fig. 3, we also use similar terms in order to obtain the target states, namely #1, #3, and #5.

[84] While the QSH and QAH states in Fig. 2 have slightly different energies, we numerically find that the two states become degenerate when the moiré potential is switched off. The symmetry that connects these states remains an open question.

[85] O. Gat and J. E. Avron, Semiclassical analysis and the magnetization of the Hofstadter model, Phys. Rev. Lett. **91**, 186801 (2003).

[86] D. Xiao, J. Shi, and Q. Niu, Berry phase correction to electron density of states in solids, Phys. Rev. Lett. **95**, 137204 (2005).

[87] T. Thonhauser, D. Ceresoli, D. Vanderbilt, and R. Resta, Orbital magnetization in periodic insulators, Phys. Rev. Lett. **95**, 137205 (2005).

[88] R. Nakai and K. Nomura, Crossed responses of spin and orbital magnetism in topological insulators, Phys. Rev. B **93**, 214434 (2016).

[89] M. Kharitonov, Phase diagram for the $\nu = 0$ quantum Hall state in monolayer graphene, Phys. Rev. B **85**, 155439 (2012).

[90] M. Kharitonov, Canted antiferromagnetic phase of the ν=0 quantum Hall state in bilayer graphene, Phys. Rev. Lett. **109**, 046803 (2012).

[91] K. Nomura, S. Ryu, and D.-H. Lee, Field-induced Kosterlitz-Thouless transition in the $n = 0$ Landau level of graphene, Phys. Rev. Lett. **103**, 216801 (2009).

[92] J. K. Jain, Composite-fermion approach for the fractional quantum Hall effect, Phys. Rev. Lett. **63**, 199 (1989).

[93] J. K. Jain, *Composite Fermions* (Cambridge University Press, New York, 2007).

[94] X. G. Wu, G. Dev, and J. K. Jain, Mixed-spin incompressible states in the fractional quantum Hall effect, Phys. Rev. Lett. **71**, 153 (1993).

[95] V. W. Scarola and J. K. Jain, Phase diagram of bilayer composite fermion states, Phys. Rev. B **64**, 085313 (2001).

[96] F. Zhang, B. Sahu, H. Min, and A. H. MacDonald, Band structure of *ABC*-stacked graphene trilayers, Phys. Rev. B **82**, 035409 (2010).

[97] L. Liu, Y. P. Feng, and Z. X. Shen, Structural and electronic properties of *h*-bn, Phys. Rev. B **68**, 104102 (2003).